Check for updates

Manipulating Charge-Transfer Kinetics of Lithium-Rich Layered Oxide Cathodes in Halide All-Solid-State Batteries

Ruizhi Yu, Changhong Wang, Hui Duan, Ming Jiang, Anbang Zhang, Adam Fraser, Jiaxuan Zuo, Yanlong Wu, Yipeng Sun, Yang Zhao, Jianwen Liang, Jiamin Fu, Sixu Deng, Zhimin Ren, Guohua Li, Huan Huang, Ruying Li, Ning Chen, Jiantao Wang,* Xifei Li,* Chandra Veer Singh,* and Xueliang Sun*

Employing lithium-rich layered oxide (LLO) as the cathode of all-solid-state batteries (ASSBs) is highly desired for realizing high energy density. However, the poor kinetics of LLO, caused by its low electronic conductivity and significant oxygen-redox-induced structural degradation, has impeded its application in ASSBs. Here, the charge transfer kinetics of LLO is enhanced by constructing high-efficiency electron transport networks within solid-state electrodes, which considerably minimizes electron transfer resistance. In addition, an infusion-plus-coating strategy is introduced to stabilize the lattice oxygen of LLO, successfully suppressing the interfacial oxidation of solid electrolyte (Li_3InCl_6) and structural degradation of LLO. As a result, LLO-based ASSBs exhibit a high discharge capacity of 230.7 mAh g^{-1} at 0.1 C and ultra-long cycle stability over 400 cycles. This work provides an in-depth understanding of the kinetics of LLO in solid-state electrodes, and affords a practically feasible strategy to obtain high-energy-density ASSBs.

1. Introduction

All-solid-state batteries (ASSBs) have attracted significant attention in recent years because of their exceptional safety and high theoretical energy density, derived from employing non-flammable inorganic solid-state electrolytes (SSEs).[1] Many inorganic SSEs based on sulfides,[2] oxides,[3] halides,[4] and borohydrides[5] have been developed over the past decades, including those demonstrating high ionic conductivity (e.g., 12 mS cm^{-1} for $Li_{10}GeP_2S_{12}$, LGPS, and 25 mS cm^{-1} for $Li_{9.54}Si_{1.74}P_{1.44}S_{11.7}Cl_{0.3}$, LSPSCl),[2] high-voltage stability (e.g., 4.21 V versus Li$^+$/Li for Li_3YCl_6, LYC, and 4.3 V versus Li$^+$/Li for Li_3InCl_6, LIC),[6] low cost (Li_2ZrCl_6 and $Li_{2.25}Zr_{0.75}Fe_{0.25}Cl_6$),[7] and appropriate mechanical properties.[8] With these advances in SSEs, various cathode materials have been attempted in ASSBs, such as $LiCoO_2$ (LCO),[9] $LiNi_{0.5}Mn_{0.3}Co_{0.2}O_2$ (NMC532),[10] and Ni-rich layered cathode materials (e.g., $LiNi_{0.8}Mn_{0.1}Co_{0.1}O_2$, NMC811,[4c] $LiNi_{0.85}Co_{0.1}Mn_{0.05}O_2$,Ni85,[11] and $LiNi_{0.90}Co_{0.05}Mn_{0.05}O_2$, Ni90[12]). These cathode materials typically show a specific capacity of <200 mAh g^{-1},[13] which limits the energy density of ASSBs to less than 450 Wh kg^{-1}.[14] Comparatively, lithium-rich layered oxide (LLO) possesses a higher theoretical capacity of ≥250 mAh g^{-1},[15] and is thus a promising candidate for achieving ASSBs with an energy density of 500 Wh kg^{-1}

R. Yu, C. Wang, H. Duan, A. Fraser, Y. Sun, Y. Zhao, J. Liang, J. Fu,
S. Deng, R. Li, X. Sun
Department of Mechanical and Materials Engineering
University of Western Ontario
London, Ontario N6A 5B9, Canada
E-mail: xsun9@uwo.ca

R. Yu
Institute of Micro/Nano Materials and Devices
Ningbo University of Technology
Ningbo, Zhejiang 315211, China

C. Wang, H. Huang, J. Wang
Glabat Solid-State Battery Inc
700 Collip Circle, London, Ontario N6G 4X8, Canada
E-mail: wangjt@glabat.com

M. Jiang
Institute of Physical Science and Information Technology
Anhui University
Hefei, Anhui 230601, China

The ORCID identification number(s) for the author(s) of this article can be found under https://doi.org/10.1002/adma.202207234.

A. Zhang, Y. Wu, Z. Ren, G. Li, J. Wang
China Automotive Battery Research Institute Co., Ltd
No. 11 Xingke East Street, Yanqi Economic Development Area,
Huairou District, Beijing 101407, China

J. Zuo, X. Li
Key Laboratory of Advanced Batteries Materials for Electric Vehicles of
China Petroleum and Chemical Industry Federation
Institute of Advanced Electrochemical Energy & School of Materials
Science and Engineering
Xi'an University of Technology
Xi'an, Shaanxi 710048, China
E-mail: xfli@xaut.edu.cn

N. Chen
Canadian Light Source
44 Innovation Boulevard, Saskatoon, Saskatchewan S7N 2V3, Canada

C. V. Singh
Department of Materials Science and Engineering
University of Toronto
Toronto, Ontario M5S 3E4, Canada
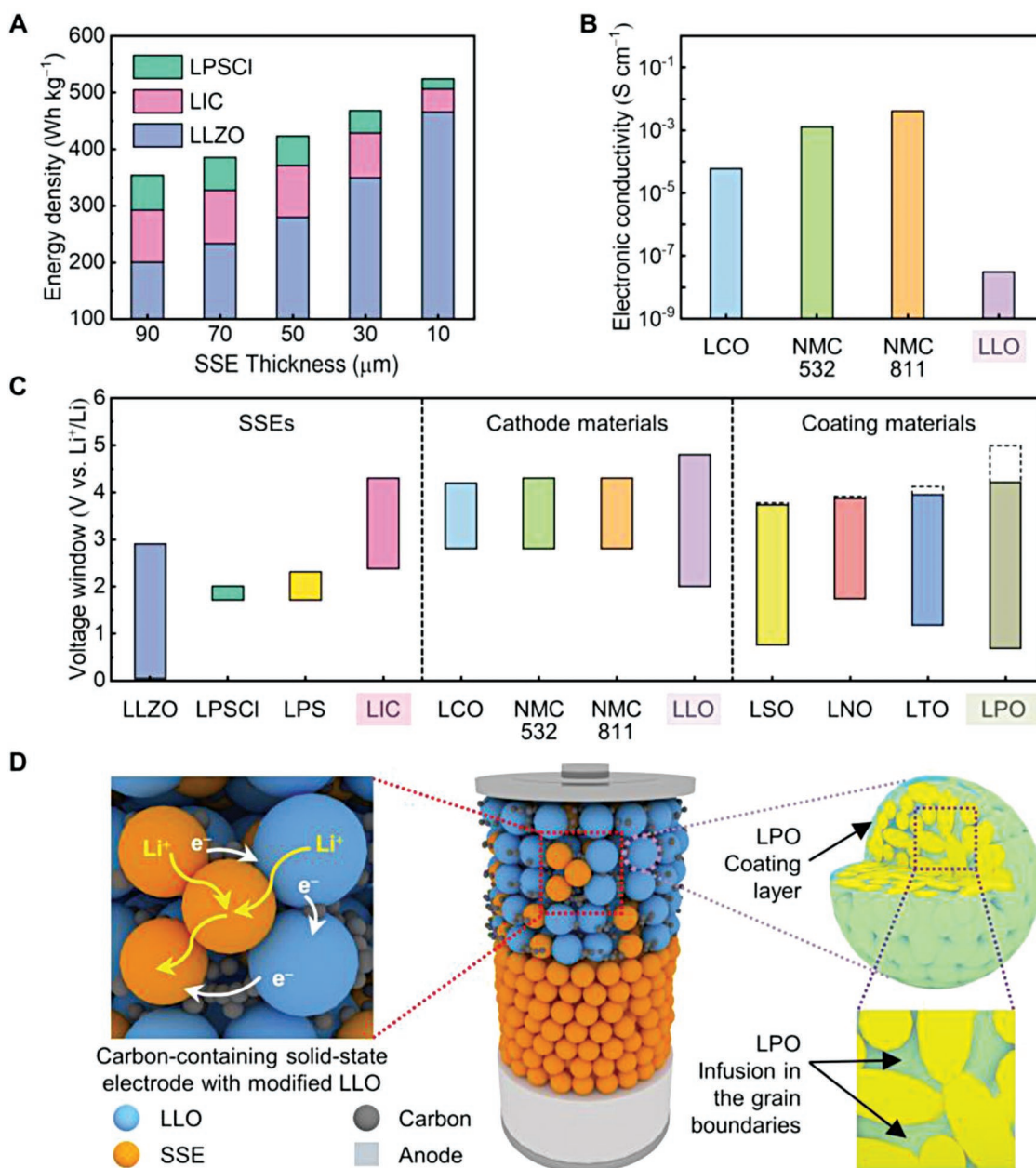E-mail: chandraveer.singh@utoronto.ca

Figure 1. Schematic for constructing ASSBs with high energy density. A) SSE thickness-dependent gravimetric energy density of LLO-based ASSBs. The capacity of the cathode sheet is 4 mAh cm^{-2} and other parameters are listed in Table S1 (Supporting Information). B) Electronic conductivities of the proposed cathode materials (LCO,[18a] NMC532,[18b] NMC811,[18b] and LLO[17b]). C) Electrochemical stability windows of proposed SSEs (Li$_7$La$_3$Zr$_2$O$_{12}$, LLZO,[3,21a] Li$_6$PS$_5$Cl, LPSCl,[21a,b] Li$_3$PS$_4$, LPS,[21a,c] and Li$_3$InCl$_6$, LIC[4c,6]), charge/discharge voltage windows of the proposed cathode materials (LCO,[18a] NMC532,[24] NMC811,[24] and LLO[17b]), and electrochemical stability windows of proposed coating materials (Li$_2$SiO$_3$, LSO, LiNbO$_3$, LNO, LiTaO$_3$, LTO, and LPO).[21a] The dashed boxes mark the potential for the compound to be fully delithiated. D) Concept of the bulk-type ASSBs enabled by carbon additives and LLO with LPO infusion-plus-coating architecture.

(**Figure 1**A; Figure S1, Supporting Information).[16] However, until now, manganese-based LLO is rarely explored in bulk-type ASSBs.

Several grand challenges that have yet to be solved hinder the application of LLO in the solid-state electrodes of ASSBs.[16c,17] First, unlike other layered oxide cathodes,[18] LLO possesses an extremely low electronic conductivity of ≈10^{-8} S cm^{-1} (Figure 1B)[17b] due to its large bandgap and the formation of charge polarons.[17b,19] Therefore, sufficient electronically conducting pathways cannot be obtained within conventional carbon-free solid-state electrodes based on LLO.[20] Second, the upper operating voltage of LLO (4.8 V vs Li$^+$/Li) greatly exceeds the intrinsic electrochemical windows of most SSEs (Figure 1C),[3,21] leading to unavoidable SSE degradation and considerable interfacial side reaction. Third, the anion redox, a unique electrochemical mechanism of LLO, generates highly

active oxygen species $O^{(2-n)-}$ $(0 < n < 2)$,[22] which may oxidize SSEs and further block interfacial lithium-ion transport. Fourth, LLO undergoes a phase transition from layered to spinel due to irreversible lattice oxygen loss.[23] This structural degradation increases interfacial resistance, and thus impedes interfacial lithium-ion transport. These perplexing interfacial issues may explain why LLO has not been successfully deployed in ASSBs until now.

In the present work, we design the solid-state electrode composition and surface chemistry of LLO to boost electron and lithium-ion transport kinetics. First, continuous electronically conducting pathways are established by introducing an appropriate amount of carbon additives into solid-state LLO electrodes. Second, an interfacial layer with high oxidative stability and satisfactory ionic conductivity—Li_3PO_4 (LPO, Figure 1C)—is constructed on LLO via an infusion-plus-coating strategy (Figure 1D), which effectively stabilizes LLO's lattice oxygen, minimizes local structural change, inhibits LLO/SSE interfacial degradation, and facilitates interfacial lithium-ion transport. As a result, LLO-based ASSBs exhibit a high initial capacity of 230.7 mAh g^{-1} and ultra-long cycling life of 431 cycles. Even at 2 C, the discharge capacity is high at 62.4 mAh g^{-1}. To the best of our knowledge, this is the first demonstrated LLO-based ASSB using a solid-state halide electrolyte (LIC). This work provides new strategies and in-depth insight into solid-state LLO electrodes and opens a new avenue for developing high-energy-density ASSBs.

2. Results and Discussion

2.1. The Electronic Conductivity of Solid-State LLO Electrodes

In this study, the halide SSE (LIC) is selected due to its higher oxidation stability (4.3 V vs Li$^+$/Li, Figure 1C) than sulfide-based SSEs (<2.31 V vs Li$^+$/Li), relatively high ionic conductivity (>10^{-3} S cm^{-1}), and moderate mechanical properties.[4c,6] In general, carbon additives are excluded in conventional solid-state electrodes to minimize side reactions between the carbon additives and SSEs.[25] Carbon-free solid-state electrodes work well with common cathode materials, (e.g., LCO, NMC532, and NMC811) because they possess high electronic conductivity above 10^{-5} S cm^{-1} (Figure 1B). However, the conventional carbon-free electrodes cannot function well when using a cathode material with low electronic conductivity (e.g., LLO and S$_8$) due to insufficient electron transport networks (**Figure 2**A).[17b] For example, a carbon-free solid-state LLO electrode can only be charged to 157.7 mAh g^{-1} and discharged to 103.7 mAh g^{-1}, and shows a considerable overpotential between charge and discharge curves (Figure 2B; Figure S2A, Supporting Information). In addition, a voltage peak at the beginning of the charging process is also identified, which is associated with an activation barrier owing to the low charge-transfer kinetics.[26] Comparatively, by adding 5% carbon additive by weight, the solid-state LLO electrode delivers a much higher charge capacity (219.7 mAh g^{-1}) and discharge capacity (166.9 mAh g^{-1}). Moreover, the solid-state LLO electrode with 5% carbon additive shows a negligible overpotential (Figure S2A, Supporting Information) and improved lithium-ion diffusion

coefficients (Figure S2B,C, Supporting Information), indicating that the electrode engineering can effectively accelerate charge-transfer kinetics. Therefore, it is essential to construct effective electron transport networks for those cathodes with low electronic conductivity such as LLO. Figure 2C displays the cycling performance of the LLO-based ASSBs at 0.2 C. Solid-state LLO electrode with 5% carbon additive exhibits a capacity retention of >60% after 100 cycles, whereas the solid-state LLO electrode with 10% carbon additive delivers fast capacity fading with a capacity retention of only 20.9%, suggesting that the detrimental effect of carbon additives on cycling performance can be minimized by controlling the carbon contents.

Direct current (DC) polarization test and linear sweep voltammetry (LSV) were performed to quantify the electronic conductivities of solid-state LLO electrodes with different contents of carbon additives. The carbon-free solid-state LLO electrode shows a low electronic conductivity of 1.20×10^{-8} S cm^{-1} (Figure 2D), implying that the limited electron transfer leads to the low capacity of the LLO-based ASSBs. With 5% and 10% carbon additives, the electronic conductivity increases to 4.09×10^{-2} (Figure 2E) and 6.89×10^{-1} S cm^{-1} (Figure 2F), respectively, suggesting that the carbon additives provide sufficient electronically conducting pathways within the solid-state LLO electrodes. However, a prominent oxidation peak at ≈4.0 V is identified in the LSV curve of the LIC electrode with 10% carbon additive (Figure 2G), indicating that excess carbon can lead to significant SSE decomposition. Therefore, an appropriate content of carbon additive with minimized detrimental influence on SSEs should be guaranteed when constructing solid-state LLO electrodes.

In situ electrochemical impedance spectroscopy (EIS) was further conducted to investigate the interfacial evolution upon cycling. The stepwise charge curves and corresponding EIS profiles are presented in Figure S3A–C (Supporting Information) and Figure 2H–J, respectively. An equivalent circuit of R(RQ)(RQ)(RQ)Q (Figure S3D, Supporting Information) is applied to fit the EIS spectra. It is well-documented that the semi-circle at high-frequency (>20 kHz), mid-frequency (20 kHz–100 Hz, indicated by dashed lines), and low-frequency (<100 Hz) regions correspond to the bulk resistance of SSE (R_{SSE}), charge-transfer resistance through cathode/SSE interface ($R_{LLO|SSE}$), and anode/SSE interfacial resistance ($R_{anode|SSE}$), respectively.[27] The most critical parameter, $R_{LLO|SSE}$, depending on the state of charge (SOC), is utilized to track the variation of interfacial properties (Figure 2K). When the charge voltage increases from 3.9 to 4.1 V, the $R_{LLO|SSE}$ value decreases, which is closely related to the adequate activation of the solid interface and the consolidation of SSE.[27a] However, the interfacial resistance of carbon-free solid-state LLO electrodes is much higher than those electrodes with 5% and 10% carbon additives, demonstrating insufficient charge-transfer pathways at the cathode/SSE interface.[27b] At further charging to 4.8 V, the $R_{LLO|SSE}$ value increases rapidly for the solid-state LLO electrode with 10% carbon additive, implying significant SSE decomposition caused by excess carbon additives. It should be noted that a noticeable increase in $R_{LLO|SSE}$ value from 4.3 to 4.6 V can be observed in both the carbon-free LLO electrode and the electrode with 5% carbon additive, which hints that the electrochemical anion redox of LLO also has considerable influence on interfacial stability.
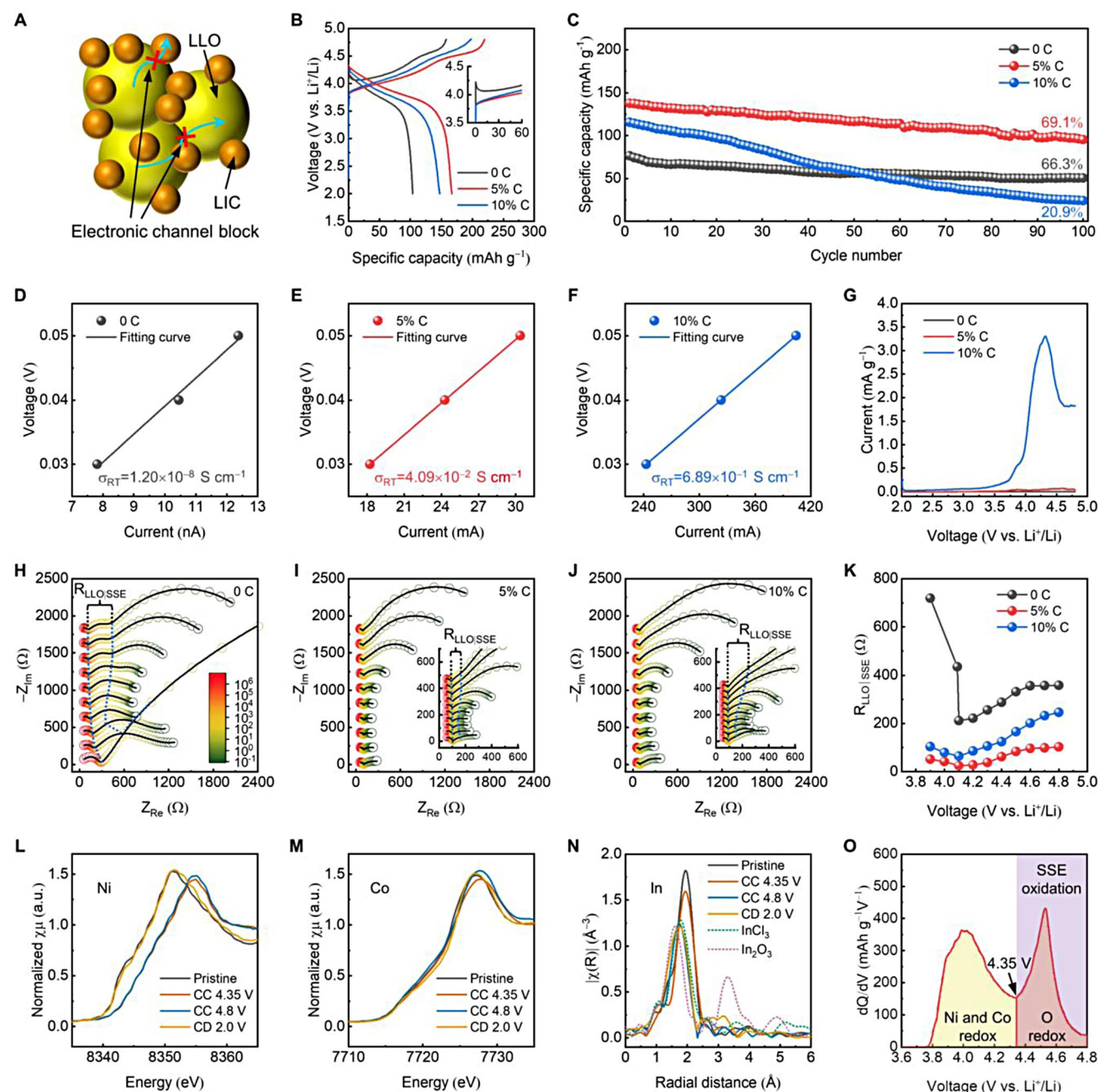
Figure 2. Effects of the intrinsic electronic conductivity and electrochemical redox of LLO on the properties of ASSBs. A) Schematic illustration of the electronic channel block around the cathode/SSE and cathode/cathode interfaces. B) Initial charge/discharge curves of the solid-state LLO electrodes with different contents of carbon additives at 0.1 C. C) Cycling performance of the solid-state LLO electrodes with different contents of carbon additives at 0.2 C. The corresponding Coulombic efficiencies are shown in Figure S8 (Supporting Information). D,F) Electronic conductivities of the solid-state LLO electrodes with 0 (D), 5% (E), and 10% (F) carbon additives. The corresponding DC polarization curves are shown in Figure S9 (Supporting Information). G) LSV profiles of the solid-state LLO electrodes with different contents of carbon additives at 0.05 mV s^{-1}. H–J) Intra-cycle impedance measurements during the initial charge cycle for the solid-state LLO electrodes with 0 (H), 5% (I), and 10% (J) carbon additives. K) Evolution of cathode/SSE interfacial resistance as a function of charge voltage in the solid-state LLO electrodes with different contents of carbon additives. L,M) Ex-situ Ni (L) and Co (M) K-edge XANES spectra of the solid-state LLO electrode with 5% carbon additive at different charge/discharge states. N) Fourier transformed In K-edge EXAFS spectra of the solid-state LLO electrode with 5% carbon additive at different charge/discharge states. The enlarged spectra between 1.0 and 2.5 Å are shown in Figure S10 (Supporting Information). The In reference spectra were collected from InCl$_3$ and In$_2$O$_3$. O) Differential capacity versus voltage (dQ/dV versus V) profile of the solid-state LLO electrode with 5% carbon additive at 0.1 C.

ADVANCED
SCIENCE NEWS

www.advancedsciencenews.com

ADVANCED
MATERIALS

www.advmat.de

2.2. Oxygen-Redox-Triggered Interfacial Degradation

Ex situ X-ray absorption spectroscopy (XAS) was performed on the solid-state LLO electrode with 5% carbon additive to probe electrochemical redox-induced interfacial structural degradation. When the cell is charged from open-circuit voltage (OCV) to 4.35 V, the X-ray absorption near edge structure (XANES) spectra of Ni (Figure 2L) and Co (Figure 2M) shift to higher energy, suggesting that Ni and Co are oxidized in this voltage range. On the contrary, no apparent change can be found in the Mn spectra (Figure S4, Supporting Information), indicating that Ni and Co redox are responsible for the capacity within the voltage range from OCV to 4.35 V.[28] When further charging to 4.8 V, the XANES spectra of Ni and Co display no edge shift. For the Mn, the white line of the XANES spectra, corresponding to the $1s \rightarrow 4p$ transition,[29] shifts to higher energy, whereas the main edge moves in the opposite direction. Furthermore, the pre-edge peak associated with the Mn $1s \rightarrow 3d$ transition transforms from a pair of splitting peaks (empty t_{2g} and e_g states) into a sharp single peak.[29,30] These changes in the Mn XANES spectra suggest the local structure distortion of the MnO_6 octahedron but no direct contribution to the capacity, indicating that oxygen anion oxidation instead of cation oxidation is mainly responsible for the voltage plateau (4.35–4.8 V).[29,30] In this high voltage plateau, highly active oxygen species, $O^{(2-n)-}$, are produced, which can easily de-coordinate from the MO_6 structure (M refers to the transition metal and Li) and chemically attack the SSEs.[31] This process results in the structural degradation of LLO and SSE oxidation. To verify the SSE oxidation, XANES spectra and extended X-ray absorption fine structure (EXAFS) spectra for the In K-edges during the charge/discharge process were collected. The XANES spectra (Figure S5, Supporting Information) display that the local environment around In changes considerably after charging from 4.35 to 4.8 V. Furthermore, the Fourier transformed In K-edge EXAFS spectra (Figure 2N) show that the average bond length of the first shell (In-Cl bond) shrinks dramatically when charging from 4.35 to 4.8 V. As the In^{3+} in the LIC cannot be further oxidized, this bond length shrinkage should be caused by the change of ligand Cl around In. At the high SOC of 4.8 V, the average bond length (≈1.72 Å) is much lower than that of a typical In-Cl (≈1.94 Å) in LIC and closer to that of a typical In-O (≈1.60 Å) in In_2O_3, suggesting the partial oxidation of LIC. The interfacial reaction product (In_2O_3) can also be determined by X-ray photoelectron spectroscopy (XPS, Figure S6, Supporting Information). During discharging, the XANES spectra of Ni and Co recover to their pristine energy, corresponding to the reduction of these ions back to their initial states. However, the white line of Mn shifts to lower than pristine energy and the pre-edge peak splitting is less resolved, indicating that the local structure around Mn ions has changed and oxygen vacancies have formed due to the side reaction at the voltage plateau.[30] More importantly, after discharging to 2.0 V, the local structure (Figure S5, Supporting Information) and average bond length of the first shell (Figure 2N) around In cannot recover to their pristine state, further validating the irreversible LIC degradation. Additionally, owing to the lower microstrain variation (0.088% at 4.8 V, Figure S7A–C, Supporting Information) of LLO during charging as compared to those of Ni-rich layered cathode materials (0.315% at 4.3 V and 0.415% at 4.6 V),[32] the morphology of solid-state LLO electrode can be maintained after cycling (Figure S7D,E, Supporting Information). Thus, the electro-chemo-microstructure coupling rather than electro-mechanics coupling, dominates the interfacial stability. Based on the above analyses, a map of the redox couples and the SSE oxidation can be illustrated as shown in Figure 2O. It can be concluded that the anion oxidation reaction leads to the interfacial structural degradation between LLO and LIC, resulting in considerable charge-transfer resistance and the low capacity of LLO in ASSBs. The local structural change and interfacial side reactions between LLO and LIC should be suppressed to secure good cycling stability, as discussed in Section 2.3.

2.3. Surface Chemistry Reconstruction to Enhance Electrochemical Performance

Here we adopted an infusion-plus-coating strategy to reconstruct the surface of LLO. LPO, as an excellent ionic conductor, possesses higher oxidation stability than conventional oxide coatings, such as LSO, LNO, and LTO, and was therefore selected as the coating layer (Figure 1C).[21a] To maximize the protective effect of LPO, atomic layer deposition (ALD) and annealing techniques were performed to construct the LLO with infusion-plus-coating architecture (LPOn-iLPO LLO, see the supplemental information for a detailed description of the process). The infusion-plus-coating architecture (**Figure 3**A) is evidenced by scanning electron microscopy (SEM), energy-dispersive X-ray (EDX) elemental mapping, and scanning transmission electron microscopy (STEM) analyses, as shown in Figures S11–S13 (Supporting Information). Moreover, X-ray diffraction (XRD) patterns (Figure S14, Supporting Information) of the bare LLO and LPO5-iLPO LLO (surface chemistry modified LLO, SCM LLO) reveal that the ALD-based infusion-plus-coating strategy do not change the stability of layered structure. The optimization procedure of the electrochemical performance for the LLO-based ASSBs is presented in Figure S15A–D (Supporting Information). It should be mentioned that the solid-state electrode contains 5% carbon additive. The SCM LLO cell demonstrates the best electrochemical performance among all modified samples. Compared with the bare LLO cell, the initial charge/discharge capacity and Coulombic efficiency are remarkably enhanced after the surface chemistry modification (Figure 3B). The high initial discharge capacity of 230.7 mAh g^{-1} and Coulombic efficiency of 83.0% for the SCM LLO cell are similar to those of liquid-based lithium-ion batteries with LLO (240.7 mAh g^{-1}, 82.8%, Figure S15E, Supporting Information). In particular, the SCM LLO cell exhibits a long voltage plateau at charge voltage between 4.35 and 4.8 V, whereas the voltage plateau is less evident in the bare LLO cell, denoting that the infusion-plus-coating architecture can stabilize the oxygen redox.[33] Furthermore, the cycling performance is improved from 69.1% to 87.9% after 100 cycles at 0.2 C (Figure 3C), and the polarization (Figure S15F,G, Supporting Information) and voltage decay (Figure S15H,I, Supporting Information) are also effectively suppressed. As shown in Figure 3D, the SCM LLO cell delivers increased rate capability, which can achieve ≈26% (62.4 mAh g^{-1}) of the capacity at 0.05 C. Even at a high
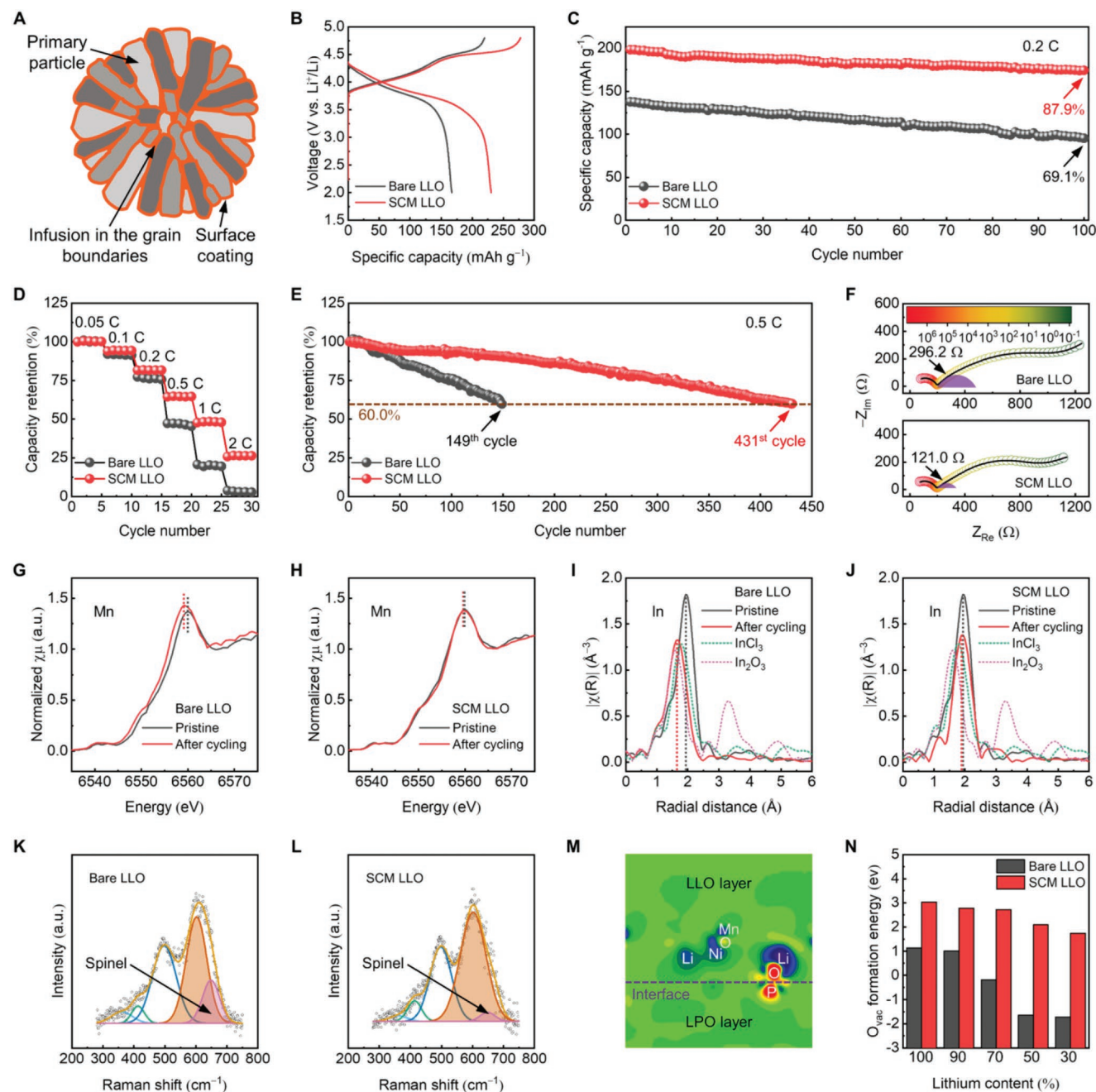
Figure 3. Understanding the improved stability in ASSBs using LLO with infusion-plus-coating architecture. A) A diagram of the infusion-plus-coating architecture, in which LPO is infused into the grain boundaries and coated on the secondary particle surface. B) Initial charge/discharge curves of the bare LLO and SCM LLO cells at 0.1 C. C) Cycling performance of the bare LLO and SCM LLO cells at 0.2 C. D) Normalized rate capabilities of the bare LLO and SCM LLO cells at different current rates. Their corresponding capacity variations at different rates are shown in Figure S15B (Supporting Information). E) Normalized long-term cycling performance of the bare LLO and SCM LLO cells at 0.5 C. Their corresponding capacity and Coulombic efficiency variations are shown in Figure S15J,K (Supporting Information). F) The Nyquist plots of the EIS spectra of the bare LLO and SCM LLO cells after 100 cycles at 0.2 C. The interfacial resistances are illustrated by colored semicircles. G,H) Mn K-edge XANES spectra of the bare LLO (G) and SCM LLO (H) electrodes at different cycling stages. I,J) Fourier transformed In K-edge EXAFS spectra of the bare LLO (I) and SCM LLO (J) electrodes at different cycling stages. The In reference spectra were collected from $InCl_3$ and In_2O_3. K,L) Raman spectra and fitted results of bare LLO (K) and SCM LLO (L) electrodes after 100 cycles at 0.2 C. M) Charge density difference of a simulated interface between the LLO (001) surface and LPO (010) surface. N) The variations of O_{vac} formation energy in the bare LLO and SCM LLO structures at different delithiation stages.

rate of 0.5 C, the SCM LLO cell exhibits long cycle life of 431 cycles, which significantly outperforms that of the bare LLO cell (149 cycles), as shown in Figure 3E. Even using a carbon-free

solid-state electrode, the SCM LLO shows an improved cycling performance (Figure S16, Supporting Information). More importantly, the infusion-plus-coating strategy can enhance the

**ADVANCED
SCIENCE NEWS**

www.advancedsciencenews.com

**ADVANCED
MATERIALS**

www.advmat.de

cycling stability of LLO in other solid-state battery system (e.g., using LYC and LLZO as SSEs, Figure S17, Supporting Information), suggesting the surface chemistry reconstruction of LLO can enhance the stability of LLO/SSE interface.

2.4. Suppressed Interfacial Structural Deterioration upon Electrochemical Cycling

EIS was conducted to evaluate the effects of surface chemistry modification on the interfacial properties during cycling (Figure 3F), and reveal the mechanism for enhanced electrochemical performance of LLO-based ASSBs. The equivalent circuit of R(RQ)(RQ)(RQ)Q (Figure S3D, Supporting Information) is applied to fit the EIS spectra. After 100 cycles at 0.2 C, the interfacial resistance $R_{LLO|SSE}$ of the SCM LLO cell is 121.0 Ω, which is much lower than that of the bare LLO cell (296.2 Ω), and therefore the improved electrochemical performance for the SCM LLO cell is ascribed to the decreased charge-transfer resistance at the cathode/SSE interface. Furthermore, XAS was employed to understand the change in interfacial resistance. The Ni (Figure S18A, Supporting Information) and Co (Figure S18B, Supporting Information) K-edge XANES spectra of the bare solid-state LLO electrode display a noticeable shift to higher energy when the cell is charged/discharged from the pristine to the 100th cycle at 0.2 C. These results indicate the oxidation of Ni and Co even after discharging to 2.0 V, whereas the changes for the solid-state SCM LLO electrode (Figure S18C,D, Supporting Information) are less prominent. The Mn K-edge XANES spectra of the bare solid-state LLO electrode (Figure 3G) show a noticeable shape change and shift to lower energy after cycling, implying significant Mn reduction and structural transformation.[31a] In contrast, the local environment around Mn in the solid-state SCM LLO electrode (Figure 3H) can be maintained well after cycling. The maintained transition metal valences in the SCM LLO electrode are connected with the stable cation-anion redox couples and high reversibility of the lithiation/delithiation process, suggesting a suppressed side reaction at the cathode/SSE interface. Moreover, in the Fourier transformed In K-edge EXAFS spectra (Figure 3I), a severe shrink of the average bond length of first shell can be observed for the bare solid-state LLO electrode, demonstrating the oxidation of SSEs. With the interfacial modification, the degeneration of SSEs in the SCM LLO electrode (Figure 3J) can be significantly mitigated during cycling, conforming the protective effect of surface chemistry modification, which can also be verified by XPS (Figure S19, Supporting Information) and time-of-flight secondary ion mass spectrometry (ToF-SIMS, Figure S20, Supporting Information).

To visualize the structural transformation of cathode materials, Raman spectra were collected for the cycled solid-state electrodes. For the LLO, the broad peak at ≈648.8 cm^{-1} is ascribed to Mn-O polyhedral distortion and shrinkage of the Mn-O bond, indicating the oxygen-release-induced phase transition from layered to spinel-like structure after cycling.[34] The ratio of spinel-like phase in the cycled solid-state SCM LLO electrode (Figure 3L) is obviously lower than that in the cycled bare solid-state LLO electrode (Figure 3K), suggesting a suppressed phase transition.

Moreover, high-resolution transmission electron microscopy (HRTEM) results show that the layered structure disappears and the spinel phase dominates on the surface of bare LLO (Figure S21A, Supporting Information) after cycling, indicating severe structural degradation. On the contrary, only a slight spinel phase can be detected, and primary layered structure can be maintained well for the SCM LLO (Figure S21B, Supporting Information). These results confirm that the surface structure of LLO can be stabilized by surface chemistry modification.

As the structural degradation at the LLO/SSE interface is highly correlated with the stability of lattice oxygen within LLO, first-principles calculations were conducted on the (001) surface of LLO as well as the interface between the (001) surface of LLO and (010) surface of LPO. Figure S22A (Supporting Information) displays the relaxed atomic structure of a LLO slab with top and bottom (001) surfaces, where the lattice oxygen is only bonded by 1) two TM (TM refers to the transition metal) and one Li (Figure S22B, Supporting Information) or 2) three TM (Figure S22C, Supporting Information). The formed Li-O-□ structure (□ symbolizes a vacancy) in configuration (1), which is similar to the highly active orphaned Li—O—Li structure, can introduce labile oxygen electrons to participate in redox activity during cycling.[35] At the interface between the LLO (001) surface and LPO (010) surface (Figure S23, Supporting Information), the lattice oxygen of LLO is bonded by the P atom and the intense electron cloud sharing demonstrates the strong covalent interaction between P and O (Figure 3M). Considering the local structure of lattice oxygen, the strong P-O bond can pull the energy of the O 2p states to the lower direction compared to the pristine lattice oxygen (Figure S24, Supporting Information), indicating reduced oxygen activity. Moreover, the formation energy of oxygen vacancy (O_{vac}) for the bare LLO and SCM LLO at different delithiation states is presented in Figure 3N. In the bare LLO structure, the O_{vac} formation energy decreases with the delithiation process and O_{vac} can be created spontaneously when the lithium content is less than 50%, as indicated by the negative value of O_{vac} formation energy. While the O_{vac} in SCM LLO is also easier to form with the delithiation process, the formation energy is constantly higher than that of bare LLO at any delithiation state, corroborating the higher stability of lattice oxygen due to surface modification.

3. Conclusion

In summary, to overcome the poor charge-transfer kinetics of LLO in conventional carbon-free solid-state electrodes (**Figure** 4A), we rationally construct electron and lithium-ion transport networks in which electronically conducting pathways are established by introducing an appropriate amount of carbon additives, and lithium-ion transport barriers are removed by reconstructing the LLO/SSE interface using an ALD-based infusion-plus-coating strategy. First, by introducing 5% carbon additive in the solid-state LLO electrodes, the discharge capacity is increased from 103.7 to 166.9 mAh g^{-1}, indicating that introducing carbon additives into solid-state electrodes with low-electronic-conductivity cathode materials can establish high-efficiency electron transfer networks
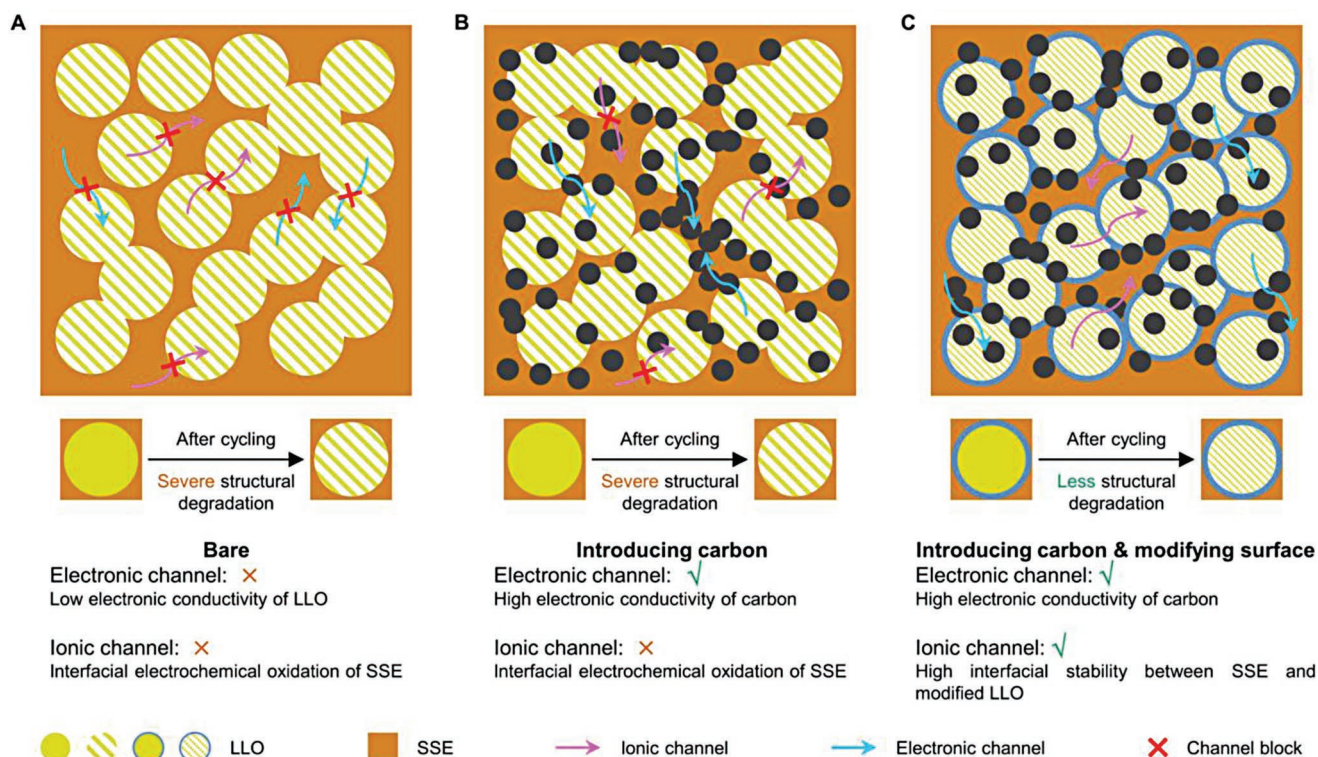
Figure 4. Schematic illustrations of the electronic and ionic migration at the interface. A) Conventional carbon-free solid-state LLO electrode. B) Carbon-containing solid-state LLO electrode. C) Carbon-containing solid-state electrode with modified LLO.

(Figure 4B). Second, an infusion-plus-coating strategy is employed to reconstruct the surface and grain boundaries of LLO by ion-conductive and high-voltage-stable LPO (Figure 4C), which not only suppresses the interfacial side reaction between LLO and the halide SSE (LIC) but also inhibits the phase degradation of LLO from layered to spinel. As a result, LLO-based ASSBs with LIC demonstrate a high discharge capacity of 230.7 mAh g^{-1} at 0.1 C and long cycle life of 431 cycles. This solid-state electrode design provides an essential reference for upgrading the electrochemical performance of other ASSBs, whose cathode materials may possess low electronic conductivity and highly active surfaces.

4. Experimental Section

Detailed information is in the Supporting Experimental Section of the Supporting Information.

Supporting Information

Supporting Information is available from the Wiley Online Library or from the author.

Conflict of Interest

The authors declare no conflict of interest.

Author Contributions

R.Y., C.W., H.D., M.J., and A.Z. contributed equally to this work. R.Y. conceptualized the study. R.Y., C.W., M.J., A.Z., Y.S., and Y.Z. were associated with methodology. R.Y., C.W., H.D., M.J., A.Z., J.Z., Y.W., J.L., J.F., S.D., Z.R., G.L., and N.C. performed investigations. R.Y. wrote the original draft. C.W., H.D., M.J., A.F., Y.S., and J.F. reviewed and edited the final manuscript. X.S. acquired funding. H.H. and R.L. acquired resources. J.W., X.L., C.V.S., and X.S. supervised the study. All authors have approved the final version of the manuscript.

Data Availability Statement

The data that support the findings of this study are available from the corresponding author upon reasonable request.

[1] a) A. Manthiram, X. Yu, S. Wang, *Nat. Rev. Mater.* **2017**, *2*, 1; b) X. Feng, H. Fang, N. Wu, P. Liu, P. Jena, J. Nanda, D. Mitlin, *Joule* **2022**, *6*, 543.

[2] a) N. Kamaya, K. Homma, Y. Yamakawa, M. Hirayama, R. Kanno, M. Yonemura, T. Kamiyama, Y. Kato, S. Hama, K. Kawamoto, A. Mitsui, *Nat. Mater.* **2011**, *10*, 682; b) Y. Kato, S. Hori, T. Saito, K. Suzuki, M. Hirayama, A. Mitsui, M. Yonemura, H. Iba, R. Kanno, *Nat. Energy* **2016**, *1*, 1.

[3] R. Murugan, V. Thangadurai, W. Weppner, *Angew. Chem. Int. Ed.* **2007**, *46*, 7778.

[4] a) T. Asano, A. Sakai, S. Ouchi, M. Sakaida, A. Miyazaki, S. Hasegawa, *Adv. Mater.* **2018**, *30*, 1803075; b) X. Li, J. Liang, J. Luo, M. N. Banis, C. Wang, W. Li, S. Deng, C. Yu, F. Zhao, Y. Hu, T.-K. Sham, L. Zhang, S. Zhao, S. Lu, H. Huang, R. Li, K. R. Adair, X. Sun, *Energy Environ. Sci.* **2019**, *12*, 2665; c) X. Li, J. Liang, N. Chen, J. Luo, K. R. Adair, C. Wang, M. N. Banis, T.-K. Sham, L. Zhang, S. Zhao, S. Lu, H. Huang, R. Li, X. Sun, *Angew. Chem. Int. Ed.* **2019**, *58*, 16427; d) J. Liang, X. Li, S. Wang, K. R. Adair, W. Li, Y. Zhao, C. Wang, Y. Hu, L. Zhang, S. Zhao, S. Lu, H. Huang, R. Li, Y. Mo, X. Sun, *J. Am. Chem. Soc.* **2020**, *142*, 7012; e) L. Zhou, C. Y. Kwok, A. Shyamsunder, Q. Zhang, X. Wu, L. F. Nazar, *Energy Environ. Sci.* **2020**, *13*, 2056; f) J. Park, D. Han, H. Kwak, Y. Han, Y. J. Choi, K.-W. Nam, Y. S. Jung, *Chem. Eng. J.* **2021**, *425*, 130630; g) J. Liang, E. van der Maas, J. Luo, X. Li, N. Chen, K. R. Adair, W. Li, J. Li, Y. Hu, J. Liu, L. Zhang, S. Zhao, S. Lu, J. Wang, H. Huang, W. Zhao, S. Parnell, R. I. Smith, S. Ganapathy, M. Wagemaker, X. Sun, *Adv. Energy Mater.* **2022**, *12*, 2103921; h) H. Kwak, S. Wang, J. Park, Y. Liu, K. T. Kim, Y. Choi, Y. Mo, Y. S. Jung, *ACS Energy Lett.* **2022**, *7*, 1776.

[5] a) S. Kim, H. Oguchi, N. Toyama, T. Sato, S. Takagi, T. Otomo, D. Arunkumar, N. Kuwata, J. Kawamura, S.-I. Orimo, *Nat. Commun.* **2019**, *10*, 1; b) J. Cuan, Y. Zhou, T. Zhou, S. Ling, K. Rui, Z. Guo, H. Liu, X. Yu, *Adv. Mater.* **2019**, *31*, 1803533.

[6] S. Wang, Q. Bai, A. M. Nolan, Y. Liu, S. Gong, Q. Sun, Y. Mo, *Angew. Chem. Int. Ed.* **2019**, *58*, 8039.

[7] a) K. Wang, Q. Ren, Z. Gu, C. Duan, J. Wang, F. Zhu, Y. Fu, J. Hao, J. Zhu, L. He, C.-W. Wang, Y. Lu, J. Ma, C. Ma, *Nat. Commun.* **2021**, *12*, 1; b) H. Kwak, D. Han, J. Lyoo, J. Park, S. H. Jung, Y. Han, G. Kwon, H. Kim, S.-T. Hong, K.-W. Nam, Y. S. Jung, *Adv. Energy Mater.* **2021**, *11*, 2003190.

[8] A. Sakuda, A. Hayashi, M. Tatsumisago, *Sci. Rep.* **2013**, *3*, 1.

[9] a) L. Wang, X. Sun, J. Ma, B. Chen, C. Li, J. Li, L. Chang, X. Yu, T.-S. Chan, Z. Hu, M. Noked, G. Cui, *Adv. Energy Mater.* **2021**, *11*, 2100881; b) C. Wang, J. Liang, M. Jiang, X. Li, S. Mukherjee, K. Adair, M. Zheng, Y. Zhao, F. Zhao, S. Zhang, R. Li, H. Huang, S. Zhao, L. Zhang, S. Lu, C. V. Singh, X. Sun, *Nano Energy* **2020**, *76*, 105015.

[10] a) C. Wang, R. Yu, S. Hwang, J. Liang, X. Li, C. Zhao, Y. Sun, J. Wang, N. Holmes, R. Li, H. Huang, S. Zhao, L. Zhang, S. Lu, D. Su, X. Sun, *Energy Storage Mater.* **2020**, *30*, 98; b) T. Wang, J. Duan, B. Zhang, W. Luo, X. Ji, H. Xu, Y. Huang, L. Huang, Z. Song, J. Wen, C. Wang, Y. Huang, J. B. Goodenough, *Energy Environ. Sci.* **2022**, *15*, 1325.

[11] L. Zhou, T.-T. Zuo, C. Y. Kwok, S. Y. Kim, A. Assoud, Q. Zhang, J. Janek, L. F. Nazar, *Nat. Energy* **2022**, *7*, 83.

[12] Y.-G. Lee, S. Fujiki, C. Jung, N. Suzuki, N. Yashiro, R. Omoda, D.-S. Ko, T. Shiratsuchi, T. Sugimoto, S. Ryu, J. H. Ku, T. Watanabe, Y. Park, Y. Aihara, D. Im, I. T. Han, *Nat. Energy* **2020**, *5*, 299.

[13] a) Y. Lyu, X. Wu, K. Wang, Z. Feng, T. Cheng, Y. Liu, M. Wang, R. Chen, L. Xu, J. Zhou, Y. Lu, B. Guo, *Adv. Energy Mater.* **2021**, *11*, 2000982; b) H.-J. Noh, S. Youn, C. S. Yoon, Y.-K. Sun, *J. Power Sources* **2013**, *233*, 121; c) J. Li, A. R. Cameron, H. Li, S. Glazier, D. Xiong, M. Chatzidakis, J. Allen, G. A. Botton, J. R. Dahn, *J. Electrochem. Soc.* **2017**, *164*, A1534; d) H.-H. Ryu, K.-J. Park, C. S. Yoon, Y.-K. Sun, *Chem. Mater.* **2018**, *30*, 1155; e) W. Mo, Z. Wang, J. Wang, X. Li, H. Guo, W. Peng, G. Yan, *Chem. Eng. J.* **2020**, *400*, 125820.

[14] C. Wang, R. Yu, H. Duan, Q. Lu, Q. Li, K. R. Adair, D. Bao, Y. Liu, R. Yang, J. Wang, S. Zhao, H. Huang, X. Sun, *ACS Energy Lett.* **2022**, *7*, 410.

[15] J.-L. Shi, J.-N. Zhang, M. He, X.-D. Zhang, Y.-X. Yin, H. Li, Y.-G. Guo, L. Gu, L.-J. Wan, *ACS Appl. Mater. Interfaces* **2016**, *8*, 20138.

[16] a) R. Malik, *Joule* **2017**, *1*, 647; b) S. Zhao, K. Yan, J. Zhang, B. Sun, G. Wang, *Angew. Chem. Int. Ed.* **2021**, *60*, 2208; c) M. Zhang, D. A. Kitchaev, Z. Lebens-Higgins, J. Vinckeviciute, M. Zuba, P. J. Reeves, C. P. Grey, M. S. Whittingham, L. F. J. Piper, A. Van der Ven, Y. S. Meng, *Nat. Rev. Mater.* **2022**, *7*, 522.

[17] a) R. Yu, M. N. Banis, C. Wang, B. Wu, Y. Huang, S. Cao, J. Li, S. Jamil, X. Lin, F. Zhao, W. Lin, B. Chang, X. Yang, H. Huang, X. Wang, X. Sun, *Energy Storage Mater.* **2021**, *37*, 509; b) M. Gao, C. Yan, Q. Shao, J. Chen, C. Zhang, G. Chen, Y. Jiang, T. Zhu, W. Sun, Y. Liu, M. Gao, H. Pan, *Small* **2021**, *17*, 2008132.

[18] a) P. Ghosh, S. Mahanty, R. N. Basu, *Mater. Chem. Phys.* **2008**, *110*, 406; b) S. Wang, M. Yan, Y. Li, C. Vinado, J. Yang, *J. Power Sources* **2018**, *393*, 75.

[19] F. Kong, R. C. Longo, M.-S. Park, J. Yoon, D.-H. Yeon, J.-H. Park, W.-H. Wang, S. Kc, S.-G. Doo, K. Cho, *J. Mater. Chem. A* **2015**, *3*, 8489.

[20] W. Zhang, T. Leichtweiß, S. P. Culver, R. Koerver, D. Das, D. A. Weber, W. G. Zeier, J. Janek, *ACS Appl. Mater. Interfaces* **2017**, *9*, 35888.

[21] a) Y. Zhu, X. He, Y. Mo, *ACS Appl. Mater. Interfaces* **2015**, *7*, 23685; b) C. Yu, S. Ganapathy, J. Hageman, L. van Eijck, E. R. H. van Eck, L. Zhang, T. Schwietert, S. Basak, E. M. Kelder, M. Wagemaker, *ACS Appl. Mater. Interfaces* **2018**, *10*, 33296; c) K. Yamamoto, S. Yang, M. Takahashi, K. Ohara, T. Uchiyama, T. Watanabe, A. Sakuda, A. Hayashi, M. Tatsumisago, H. Muto, A. Matsuda, Y. Uchimoto, *ACS Appl. Energy Mater.* **2021**, *4*, 2275.

[22] a) E. McCalla, A. M. Abakumov, M. Saubanère, D. Foix, J. Berg Erik, G. Rousse, M.-L. Doublet, D. Gonbeau, P. Novák, G. Van Tendeloo, R. Dominko, J.-M. Tarascon, *Science* **2015**, *350*, 1516; b) K. Luo, M. R. Roberts, N. Guerrini, N. Tapia-Ruiz, R. Hao, F. Massel, D. M. Pickup, S. Ramos, Y.-S. Liu, J. Guo, A. V. Chadwick, L. C. Duda, P. G. Bruce, *J. Am. Chem. Soc.* **2016**, *138*, 11211; c) R. A. House, G. J. Rees, M. A. Pérez-Osorio, J.-J. Marie, E. Boivin, A. W. Robertson, A. Nag, M. Garcia-Fernandez, K.-J. Zhou, P. G. Bruce, *Nat. Energy* **2020**, *5*, 777.

[23] a) P. Yan, J. Zheng, Z.-K. Tang, A. Devaraj, G. Chen, K. Amine, J.-G. Zhang, L.-M. Liu, C. Wang, *Nat. Nanotechnol.* **2019**, *14*, 602; b) A. Grenier, G. E. Kamm, Y. Li, H. Chung, Y. S. Meng, K. W. Chapman, *J. Am. Chem. Soc.* **2021**, *143*, 5763.

[24] Y. Xia, J. Zheng, C. Wang, M. Gu, *Nano Energy* **2018**, *49*, 434.

[25] a) F. Strauss, T. Bartsch, L. de Biasi, A. Y. Kim, J. Janek, P. Hartmann, T. Brezesinski, *ACS Energy Lett.* **2018**, *3*, 992; b) P. Minnmann, L. Quillman, S. Burkhardt, F. H. Richter, J. Janek, *J. Electrochem. Soc.* **2021**, *168*, 040537; c) W. Jiang, X. Zhu, R. Huang, S. Zhao, X. Fan, M. Ling, C. Liang, L. Wang, *Adv. Energy Mater.* **2022**, *12*, 2103473.

[26] C. L. Bender, P. Hartmann, M. Vračar, P. Adelhelm, J. Janek, *Adv. Energy Mater.* **2014**, *4*, 1301863.

[27] a) W. Zhang, D. A. Weber, H. Weigand, T. Arlt, I. Manke, D. Schröder, R. Koerver, T. Leichtweiss, P. Hartmann, W. G. Zeier,

J. Janek, *ACS Appl. Mater. Interfaces* **2017**, *9*, 17835; b) B. Zahiri, A. Patra, C. Kiggins, A. X. B. Yong, E. Ertekin, J. B. Cook, P. V. Braun, *Nat. Mater.* **2021**, *20*, 1392.

[28] a) H. Koga, L. Croguennec, M. Ménétrier, P. Mannessiez, F. Weill, C. Delmas, S. Belin, *J. Phys. Chem. C* **2014**, *118*, 5700; b) C. Cui, X. Fan, X. Zhou, J. Chen, Q. Wang, L. Ma, C. Yang, E. Hu, X.-Q. Yang, C. Wang, *J. Am. Chem. Soc.* **2020**, *142*, 8918.

[29] J. Rana, R. Kloepsch, J. Li, T. Scherb, G. Schumacher, M. Winter, J. Banhart, *J. Mater. Chem. A* **2014**, *2*, 9099.

[30] S. Tao, W. Huang, S. Chu, B. Qian, L. Liu, W. Xu, *Mater. Today Phys.* **2021**, *18*, 100403.

[31] a) E. Hu, X. Yu, R. Lin, X. Bi, J. Lu, S. Bak, K.-W. Nam, H. L. Xin, C. Jaye, D. A. Fischer, K. Amine, X.-Q. Yang, *Nat. Energy* **2018**, *3*, 690; b) G. Assat, J.-M. Tarascon, *Nat. Energy* **2018**, *3*, 373.

[32] a) R. Robert, P. Novák, *J. Electrochem. Soc.* **2015**, *162*, A1823; b) C. R. Fell, D. Qian, K. J. Carroll, M. Chi, J. L. Jones, Y. S. Meng, *Chem. Mater.* **2013**, *25*, 1621.

[33] T. Lin, T. U. Schulli, Y. Hu, X. Zhu, Q. Gu, B. Luo, B. Cowie, L. Wang, *Adv. Funct. Mater.* **2020**, *30*, 1909192.

[34] X. Ding, D. Luo, J. Cui, H. Xie, Q. Ren, Z. Lin, *Angew. Chem. Int. Ed.* **2020**, *59*, 7778.

[35] D.-H. Seo, J. Lee, A. Urban, R. Malik, S. Kang, G. Ceder, *Nat. Chem.* **2016**, *8*, 692.